Biosensors and Bioelectronics 118 (2018) 160–166

Contents lists available at ScienceDirect

Biosensors and Bioelectronics

journal homepage: www.elsevier.com/locate/bios

Target-triggered signal-on ratiometric electrochemiluminescence sensing of PSA based on MOF/Au/G-quadruplex

Kang Shao[1], Biru Wang[1], Axiu Nie, Shiyi Ye, Jing Ma, Zhonghua Li, Zhicheng Lv, Heyou Han*

State Key Laboratory of Agricultural Microbiology, College of Science, Huazhong Agricultural University, Wuhan 430070, PR China

ARTICLE INFO

Keywords:
Electrochemiluminescence
Ratiometric, amplification
Metal-organic framework
Prostatic specific antigen

ABSTRACT

Signal-amplified ratiometric electrochemiluminescence (Sa-RECL) provides an attractive approach to maximize signal-to-noise ratio through enhancing signals and eliminate interferences. In this work, we prepared a novel metal-organic framework (MOF)/Au/G-quadruplex as both quenchers and enhancers to fabricate a target-triggered ratiometric ECL sensor for high sensitive and accurate detection of prostatic specific antigen (PSA). The ratiometric ECL sensor using the dual-potential-dependent ECL emitters (quantum dots (QDs) and luminol) and MOF/Au/G-quadruplex not only achieved signal self-calibration but also realized cooperative amplification. After the sequential hybridization among of complementary DNA-QDs, PSA aptamer and pDNA-Au-Hemin-MIL-DNAzyme and the further competition of PSA, the pDNA-Au-Hemin-MIL-DNAzyme probe would keep away from the electrode surface, causing a switchover of their ECL signals from "off-on" state to "on-off" state. The ratiometric ECL aptasensor exhibits high-sensitive and accurate analytical performance toward PSA with a linear detection range from 0.5 to 500 ng mL^{-1} and a detection limit of 0.058 ng mL^{-1} (S/N = 3). The novel ratiometric ECL biosensor has been successfully applied to determine different serum samples of PSA, indicating its potential application in the clinical diagnosis.

1. Introduction

Prostate-specific antigen (PSA), a single chain polypeptide containing 237 amino acids, is the most sensitive biomarker of prostate cancer (the second primary cause of cancer mortality in many developed countries) (Perfezou et al., 2012; Jayanthi et al., 2017). Early detection of PSA provides a great promise for prostate cancer forecast, screening, diagnosis, monitoring and prognosis analysis though investigating the presence, absence or change in the level of them during each stages (Wu et al., 2007). Up to now, a variety of analytical techniques have been employed for detection of PSA, such as enzyme-linked immunosorbent assay (ELISA) (Lang et al., 2014), polymerase chain reaction (PCR) (Gerhard et al., 1994), fluorometric (Miao et al., 2016), electrochemical (Rong et al., 2016) and surface enhancement raman (SERS) (Feng et al., 2017) analysis. Electrochemiluminescence (ECL), an electrochemical redox-induced light emission, has attracted increasing interest in cancer detection due to its inherent advantages of low background interference, simple operation, high sensitivity and space-time controllability. As the optimization of the ECL detection system to maximize the signal-to-noise ratio is critical for cancer early diagnose because of low-abundance contents of targets and high interference from non-targets in biofluids as well as considerable physical differences among patients.

The employment of signal amplification can effectively maximize the analytical sensitivity of ECL. In general, there are two primary principles to achieve signal amplified ECL sensing: (i) increasing the number of signal labels in a single immunization event; (ii) improving the efficiency of a single signal label during an ECL process, especially, enhancing the ECL co-reactant and/or electrochemical activity. Carriers (metal-based (Lei and Ju, 2012), carbon-based (Liu et al., 2011; Xu et al., 2011), silica-based nanometerial (Chen et al., 2013; Qi et al., 2013), organic polymer, biomolecule etc.) amplification, bridges (antigen-antibody, aptamer-target, DNA-DNA, biotin-avidin, host-guest, mannose-lectin, etc.) (Shao et al., 2014, 2017) amplification and catalytic amplification (Li et al., 2012) are three most widely used ways to improve the number or/and efficiency of ECL signal labels (Cao et al., 2012; Li and Cui, 2013; Tian et al., 2010). Despite many alternative signal amplification strategies have been developed and achieved the expected sensitivity, false positive or negative errors still occur during the detection of trace level analytes due to instrumental efficiency or some environmental change (Jiang et al., 2014). Thus, how to ensure the accuracy of these signal-amplified methods is also a major issue to

* Corresponding author.
E-mail address: hyhan@mail.hzau.edu.cn (H. Han).
[1] Contributed equally to this work.

https://doi.org/10.1016/j.bios.2018.07.029
Received 16 April 2018; Received in revised form 24 June 2018; Accepted 15 July 2018
Available online 17 July 2018
0956-5663/

be addressed.

Ratiometric assay provides an ideal approach to eliminate these interference factors via built-in self-calibration and precise measurement to normalize variation in environmental changes (Wu et al., 2016). Xu's group firstly utilized two different potential-dependented CdS nanocrystals (−1.25 V) and luminol (+0.45 V) to achieve high-precision ratiometric ECL biosensing (Cheng et al., 2014; Zhang et al., 2013). However, scarce dual potential-dependented ECL emitters and disadvantageous cross-reaction devoted researcher to seek novel mated ECL emitters, such as C_3N_4/luminol (Wang et al., 2016), graphene quantum dots (QDs)/luminol (Zhao et al., 2015), CdTe QDs/Ru(II) complex (Fu et al., 2017), CdTe QDs/polymer dots (Chen et al., 2017), $Ru(bpy)_3^{2+}$/$Ir(ppy)_3$ (Wang et al., 2017b), Ru/Os complex (Sun et al., 2015) etc.. Particularly, the bipolar electrode and array electrode (Feng et al., 2016b) formed by physically separation of working interface provids new perspectives to achieve spatial-resolved ratiometric (Wang et al., 2017c) and multicolor ECL with no need of common coreactants (eg. C_3N_4/$Ru(bpy)_3^{2+}$ (Feng et al., 2016a), luminol/$Ru(bpy)_3^{2+}$ (Zhang et al., 2016), etc.). Unfortunately, there is little attention on seeking near-infrared ECL emitters and integrating signal amplification with ratiometric assay to maximum the signal-to noise ratio (Hao et al., 2014). Most recently, our group utilized graphene/gold nanorods/G-quadruplex intermediate to construct a novel ECL aptasensor with ultrahigh sensitivity and accuracy based on the incorporated advantages of near-infrared emission, signal amplification and ratiometry (Shao et al., 2016). Unsatisfactorily, the “sandwich” sensing mode is difficult to avoid the nonspecific adsorption of probe, which may bring few unescapable errors. Therefore, exploring the new dual-role probe and avoiding the nonspecific adsorption are necessary but remains big challenges.

Inspired by the recent reports on quencher and carrier characters of Fe-based metal–organic framework (MOF) (Fang et al., 2014; Wang et al., 2017a; Xie et al., 2015) and the previous research studies on ratiometric ECL, we prepared a MOF/Au/G-quadruplex dual-role intermedium to fabricate a target-triggered ratiometric ECL sensors for achieving both high sensitive and accurate detection of PSA based on the “competition” model. The near-infrared (NIR) CdSe/ZnS quantum dots (QDs) and luminol as the matched dual potential-dependented ECL emitters output two diacritical signals locating at ~− 1.5 V and + 0.45 V, respectively. Based on Roggan’ findings that the absorption minimum of fully deoxygenated whole blood was at 805 nm and maximas was at 420 and 540 nm, NIR QDs with optimal emission at 675 nm can minimize the autofluorescence of whole blood and tissue (Roggan et al., 1999; Dennany et al., 2008). The Fe-MIL-88 MOF was saved as the carrier platform to encapsulate a good deal of hemin molecule and further fix G-quadruplex DNAzyme for achieving synergetic catalytic amplification of luminol. The ECL quenching of NIR QDs by Fe-MIL-88 MOF was first investigated and applied in the ratiometric ECL sensors. The novel ratiometric strategy has been successfully applied in serum samples for PSA and possessed significant potential application in the clinical diagnosis.

2. Materials and methods

The materials and reagents were presented in Supporting information.

2.1. Preparation of Fe-MIL-88 MOF, Hemin-MIL and Au-Hemin-MIL composites

Fe-MIL-88 MOF was prepared according to the previous method (Xie et al., 2015). Briefly, 0.692 mmol of $FeCl_3{\cdot}6H_2O$ and 0.692 mmol of 2-amino-terephthalic acid were dissolved in 15 mL of DMF and 35 mmol acetic acid was then added into this mixed solution after heating for 15 min. The mixed solution was placed in an oil bath at 120 °C for 4 h. After cooling to room temperature, the crude products were purificated by centrifugation and washed with DMF and ethanol. Finally, the Fe-MIL-88 MOF was dried in a vacuum oven. Hemin-MIL composites were synthesized with a similar method for Fe-MIL-88 MOF, except that 0.692 mmol $FeCl_3{\cdot}6H_2O$ was replaced by 0.346 mmol hemin and 0.346 mmol $FeCl_3{\cdot}6H_2O$ in the current work.

Hemin-MIL/AuNPs composites (Au-Hemin-MIL) were prepared by electrostatic self-assembly. 100 μL PEI solution (20 mg mL^{-1}) was slowly added to 1 mL Hemin-MIL solution (1 mg mL^{-1}) with stirring for 12 h (500 r.p.m), and then washed 3 times with deionized water and dispersed the precipitate into 2 mL of water. 100 μL AuNPs solution was added to the above dispersion and stand for several hours. The precipitates were washed several times and dispersed to deionized water for the standby application.

2.2. Preparation of pDNA-Au-Hemin-MIL-DNAzyme bioconjugate

First, the G-quadruplex (120 μL, 1 μM) was activated with 1.35 μL of TCEP solution (10 mM) for one hour, which aim to reduce disulfide bonds, followed by mixed it with pDNA (15 μL, 1 μM). Then 250 μL of 2.0 mg mL^{-1} Au-Hemin-MIL were added into the mixture for incubating 16 h (37 °C)to obtain G-quadruplex and pDNA modified Au-Hemin-MIL composites. A salt-stabilization in 0.1 M NaCl, 1% BSA was added to the resulting solution to block the unreacted active sites of Au-Hemin-MIL. After centrifugation, the obtained product was redispersed in 500 μL of 0.1 M PBS containing 0.1 M of KCl. Then, 20 μL of hemin (0.1 mM) was added to the suspension and incubated for 2 h in the dark to form a Au-Hemin-MIL-DNAzyme probe, and the redundant hemin was removed by centrifugation. The obtained probe was dispersed into 0.1 M PBS containing 0.1 M KCl and stored at 4 °C for further use.

2.3. Fabrication of the ECL aptasensor

The preparation process of the aptasensor was described in Scheme 1B. 5 μL of purified CdSe/ZnS QDs solution was dropcast on the pretreated polished glassy carbon electrodes (GCE, diameter of 3 mm) and let them dry out in the air at room temperature to obtain GCE modified by the QDs film. Then, 10 μL of EDC (10 mg mL^{-1}) and NHS (20 mg mL^{-1}) mixed solution was dripped over the surface of QDs/GCE for incubating 1 h at 37 °C to activate the -COOH of QDs. After rinsing the QDs/GCE with PBST, the activated QDs/GCE was immersed in 100 μL of amino-modified cDNA for over 12 h (4 °C), followed by thoroughly washing. 10 μL of PSA aptamer was driped onto the electrode surface for incubation 2 h at 37 °C. Then, the electrode was washed with PBST and blocked with 0.5% BSA. After that, 10 μL of cDNA-Au-Hemin-MIL-DNAzyme bioconjugate was driped over the GCE surface to react for 2 h at 37 °C. The GCE was incubated in 100 μL of PSA antigen for 1 h (37 °C) and washed thoroughly with PBST. Finally, the modified GCE was measured by ECL analyzer in the PBS (0.1 M, pH 8.0) containing 1 mM of H_2O_2 with a potential range from − 1.5–0.5 V and a scan rate of 300 mV s^{-1}.

3. Results and discussion

3.1. Characterization of pDNA-Au-Hemin-MIL-DNAzyme probes and related materials

The preparation of Au NPs with different sizes and NIR QDs were presented in Supporting information. Au NPs prepared by sodium borohydride reduction reaction and sodium citrate reduction reaction are about 3 nm and 20–30 nm in size, respectively (Fig. S1 and S2). Scheme 1A shows the preparation process of pDNA-Au-Hemin-MIL-DNAzyme bioconjugate. A Hemin-MIL complex was synthesized by replacing hemin with half of the molar amount of $FeCl_3{\cdot}6H_2O$ using a similar method of preparing Fe-MIL-88 MOF. Afterwards, Au-Hemin-MIL nanocomposites were prepared by successively encapsulating cationic polymer PEI and adsorbing AuNPs. Finally, the DNAs consisting

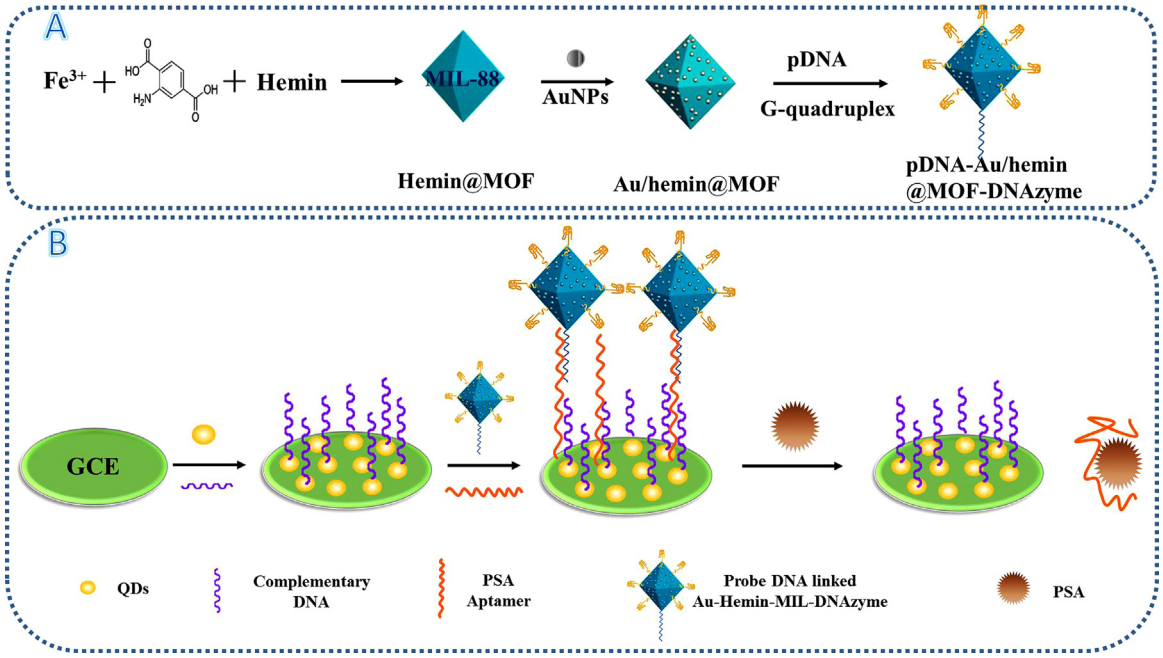

Scheme 1. (A) Schematic illustration of fabrication procedures of MOF/Au/G-quadruplex and (B) signal-switchable ECL aptasensor for detection of PSA.

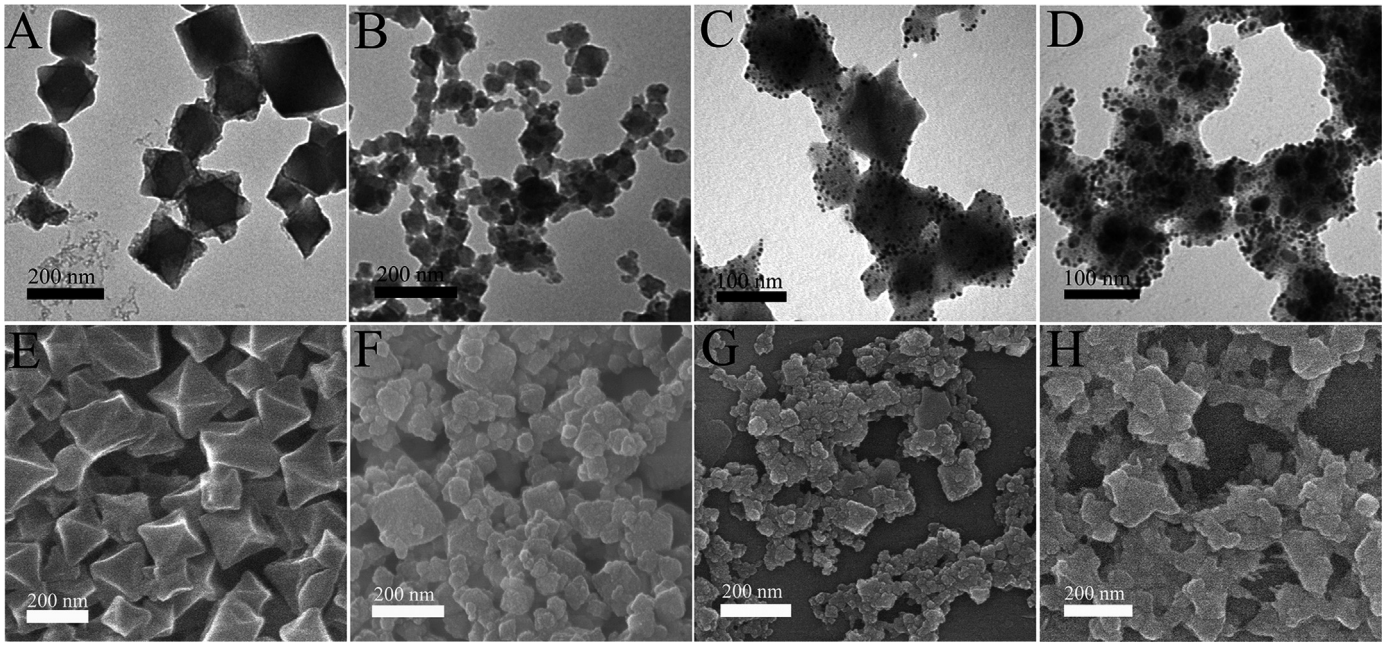

Fig. 1. TEM images of (A) NH_2-MIL, (B) Hemin-MIL, (C) Au-Hemin-MIL, (D) pDNA-Au-Hemin-MIL-DNAzyme. SEM images of (E) NH_2-MIL, (F) Hemin-MIL, (G) Au-Hemin-MIL, (H) pDNA-Au-Hemin-MIL-DNAzyme.

of probe DNA and G-quadruplex was modified on Au-Hemin-MIL, and the resulting pDNA-Au-Hemin-MIL-DNAzyme bioprobe can not only retain the morphology and properties of MOF, but also gain a synergetic catalytic activity from hemin and DNAzyme. Through the TEM and SEM images (Fig. 1A and E), it can be seen that Fe-MIL-88 MOF exhibits a regular octahedral morphology with an average particle size of about 200 nm, roughly corresponding to data of hydrodynamic size (Fig. S3). If hemin was used to replace a part of the metal ion source, it can be seen that the morphology of the prepared Hemin-MIL material has undergone a slight change and the particle size tends to be less than 100 nm roughly in keep with data of hydrodynamic size (Fig. S4), indicating that the incorporation of hemin in Fe-MIL-88 has a weak influence on the nucleation or/and crystal growth of MOF (Fig. 1 B and F). The XRD pattern of Hemin-MIL (red line) is similar to MIL (black line) with five diffraction peaks at 9.03, 11.5, 16.4, 17.8 and 18.6 indexed to the (002), (101), (103), (200) and (201) planes (Fig. S5), which also confirmed the above conclusion. The Au NPs were loaded onto the surface of the Hemin-MIL material via the PEI cross-linking process. From Fig. 1 C and G, it can be clearly seen that the surface of Hemin-MIL was anchored a large amount of Au NPs. After the modification of DNA Au-Hemin-MIL with pDNA and G-quadruplex through bonding interaction Au atoms and –SH group, a slight morphology change of the composites can be observed clearly in Fig. 1D and H. In addition, the increased adhesion or aggregation among of nanoparticles

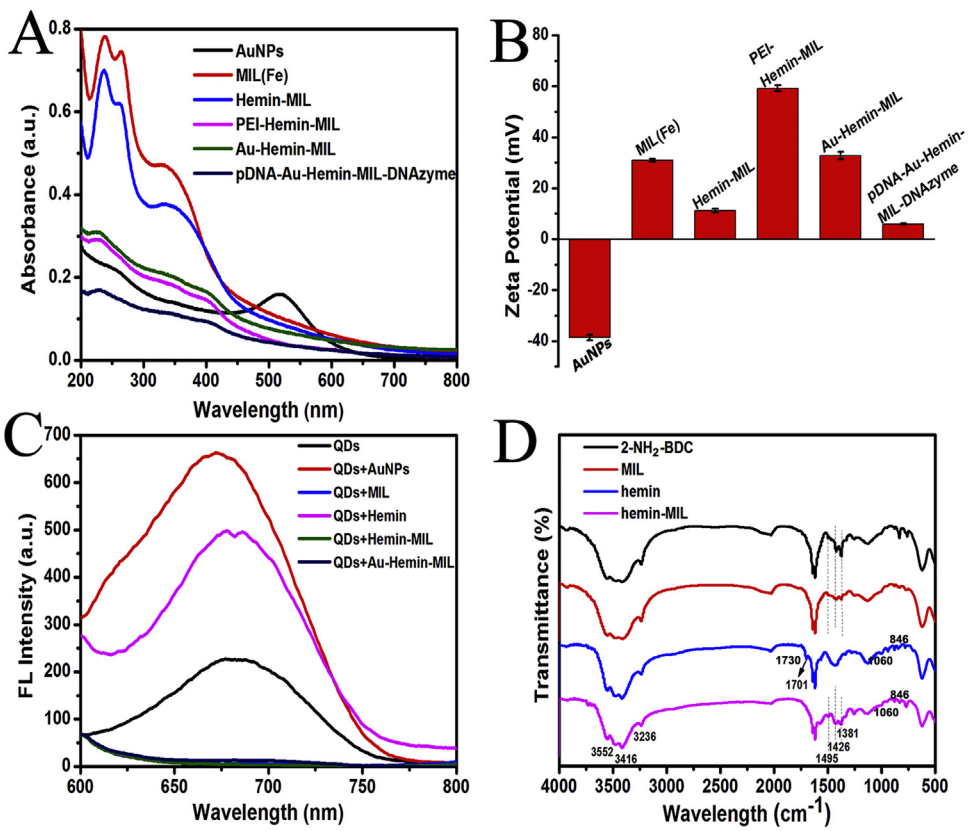

Fig. 2. (A) UV–vis absorption spectra of AuNPs, Fe-MIL, Hemin-MIL, PEI-Hemin-MIL, Au-Hemin-MIL, pDNA-Au-Hemin-MIL-DNAzyme. (B) Zeta potential of AuNPs, Fe-MIL, Hemin-MIL, PEI-Hemin-MIL, Au-Hemin-MIL, pDNA-Au-Hemin-MIL-DNAzyme. (C) Fluorescence spectra of QDs (a) after identical addition of AuNPs (b), Fe-MIL (c), Hemin (d), Hemin-MIL (e) and Au-Hemin-MIL (f). (D) FT-IR spectra of 2-amino-terephthalic acid, MIL, hemin and Hemin-MIL.

can also indicate the successful preparation of pDNA-Au-Hemin-MIL-DNAzyme bioconjugate.

For further proving the successful preparation of the pDNA-Au-Hemin-MIL-DNAzyme bioconjugate, the UV–Vis and zeta potential were used to characterize the components in the complex. As shown in Fig. 2A, due to surface plasmon resonance, Au NPs exhibit strong UV characteristic absorption peaks at 517 nm. The prepared Fe-MIL-88 MOF shows a strong UV–vis absorption peak at 238 nm. Due to the addition of hemin, the Hemin-MIL complex shows another absorption peak at 335 nm. Comparing the UV–vis absorption spectra of PEI-Hemin-MIL and Au-Hemin-MIL, we can observe that the absorbance at Au-Hemin-MIL at 517 nm is significantly greater than that at PEI-Hemin-MIL. After the modification with the DNA strand, the characteristic absorption peak of the DNA can be found at 260 nm. These results also indicate the successful formation of pDNA-Au-Hemin-MIL-DNAzyme bioconjugate. In addition, as shown in Fig. 2B, the surface of the AuNPs is negatively charged by the Zeta potential test. The Zata potentials of the MIL and Hemin-MIL are + 30.9 and + 11.2 mV, respectively. In contrast, PEI-Hemin-MIL shows a stronger positive charge potential value of 59.2 mV by adsorbing the cationic polymer PEI. After negatively charged AuNPs and DNA strands were modified one after the other, the complexes showed a very weak positive potential value of 5.93 mV. The obvious change in the potential results indicates the successful assembly of the bioconjugate.

The successfully preparation of Fe-MIL-88 MOF and Hemin-MIL composites can be further confirmed by fourier transform infrared (FT-IR) spectroscopy. As is shown in Fig. 2D, the strong band of each material at 3416 cm^{-1} is caused by the stretching vibration of the O-H bond in the carboxyl group. Compared with hemin (blue curve), due to the successful coordination of carboxyl groups and iron ions, no characteristic peak of stretching vibration of C=O in carboxyl functional groups at 1701 cm^{-1} was observed in FT-IR spectra of Fe-MIL-88 and Hemin-MIL. In addition, due to the coordination of oxygen atoms in DMF and iron ions, new characteristic peaks were observed at 1495 cm^{-1} for Fe-MIL-88 MOF (red curve) and Hemin-MIL complex (rose-red curve). The above results of FT-IR spectra indicate that Hemin can partially replace $FeCl_3 \cdot 6H_2O$ as a metal ion source for MOF materials, and also confirmed the successful synthesis of Fe-MIL-88 MOF and Hemin-MIL composites. After successful preparation of Au-Hemin-MIL nanocomposites, it is necessary to study their influence on the optical properties of QDs. The effects of Au NPs, Fe-MIL-88, Hemin, Hemin-MIL, and Au-Hemin-MIL nanomaterials on the fluorescence properties of quantum dots were explored in this experiment while keeping the same amount of the added substance materials. As shown in Fig. 2C, the pure quantum dot solution has a strong fluorescence emission peak at 675 nm. After the Au NPs or Hemin was added to the quantum dot solution, the fluorescence intensity of QDs increased a lot. However, after adding MIL, Hemin-MIL or Au-Hemin-MIL to the solution, it can be seen from the figure that the fluorescence emission peak of QDs at 675 nm almost disappears. These results are in step with the data of luminescence photos of QDs, QDs + AuNPs, QDs + MIL, QDs + hemin, QDs + Hemin-MIL and QDs + Au-Hemin-MIL under ultraviolet irradiation (Fig. S6), indicating good fluorescence quenching effects on QDs of the MIL, Hemin-MIL and Au-Hemin-MIL.

To demonstrate that pDNA and G-quadruplexes were successfully modified onto the Au-Hemin-MIL, the Fe, Au, C, O, N, P, and S elements in the pDNA-Au-Hemin-MIL-DNAzyme sample were investigated though X-ray photoelectron spectroscopy (XPS). (Fig. S7). The peak at 711.28 eV in the spectrum belongs to Fe 2p, which may originate from the hemin and MIL in the composites. The strong peak appearing in the energy spectrum at 399.68 eV is ascribed to N 1 s, and its source may also be an organic ligand molecule in hemin and MOF. The energy spectrum peaks at 95.28 eV, 132.18 eV, and 163.73 eV are attributed to Au 4 f, P 2p, and S 2p, respectively. Au 4 f originates from Au-Hemin-MIL, but pure Au-Hemin-MIL does not contain P and S elements. Thus P and S elements are derived from thiol-modified pDNA and G-quadruplex. The above results directly confirms the successful preparation of pDNA-Au-Hemin-MIL-DNAzyme.

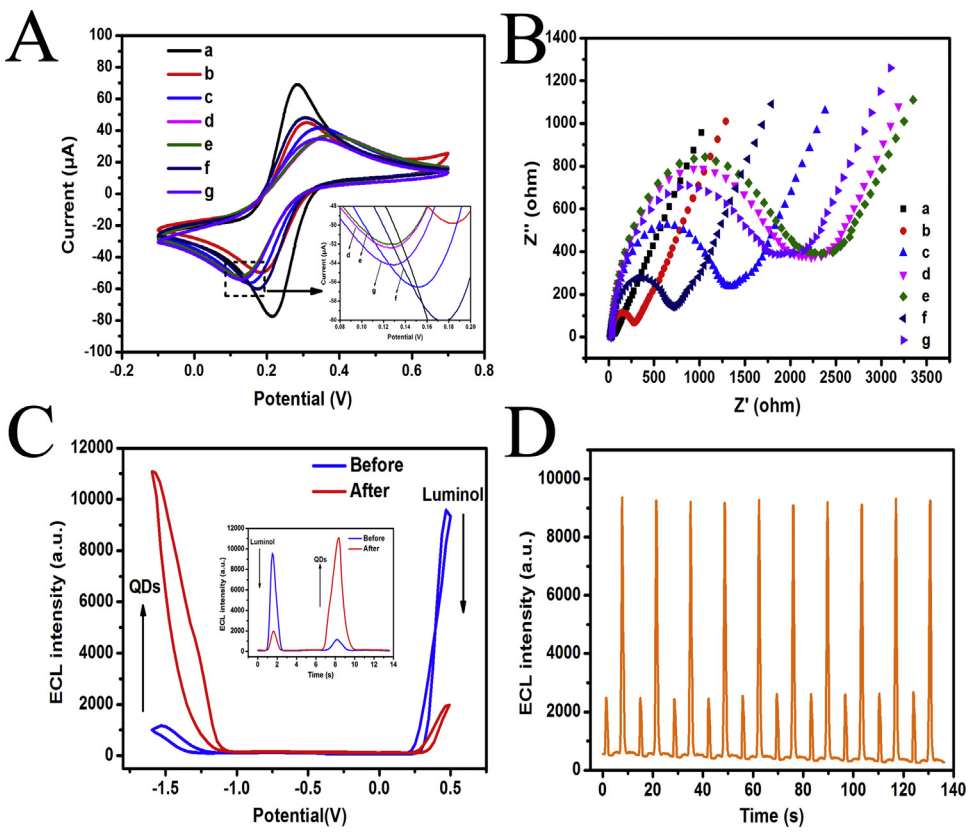

Fig. 3. CV (A) and EIS (B) of (a) bare GCE, (b) QDs/GCE, (c) cDNA/QDs/GCE, (d) Aptamer/cDNA/QDs/GCE, (e) block/Aptamer/cDNA/QDs/GCE, (f) pDNA-Au-Hemin-MIL-DNAzyme/block/Aptamer/cDNA/QDs/GCE, (g) PSA/pDNA-Au-Hemin-MIL-DNAzyme/block/ Aptamer/cDNA/QDs/GCE at the PSA concentration of 10 ng mL^{-1}. (C) ECL responses before and after incubating with PSA. (D) ECL signal stability.

3.2. Characterization of the ECL immunosensor

In order to verify the successful assembly of the RECL sensor, we conducted electrochemical cyclic voltammetry (CV) and electrochemical impedance spectroscopy (EIS) tests, respectively. The construction of the sensor is inferred by a change in its peak current and resistance signal. The CV test was first performed at a scan rate of 100 mV/s from − 0.1 to 0.7 V in the electrolyte solution contained 5.0 mM of $[Fe(CN)_6]^{3-/4-}$ and 0.1 mM of KCl using the typical three-electrode system. As shown in Fig. 3A, the CV curve of the bare electrode shows a pair of reversible redox peaks (curve a). After a layer of quantum dots is decorated on the surface of the bare electrode, the peak current of the electrode is reduced and the oxidation peak is reduced. The potential difference (ΔE) between the reduction peaks increases significantly (curve b). The reason for this phenomenon is that the conductivity of the sensor is weakened by semiconductor quantum dot which can hinder the electron transfer process at the electrode interface. With continuous assembly of cDNA, PSA aptamers, and blocking agents (curves c, d, e), the measured peak currents of the sensor are continuously weakened, and the potential differences are further increased, which is ascribed to the blocking effect of the blocking protein and electrostatic repulsion between the phosphate backbone and the electroactive probe. However, when the electrode is assembled with a pDNA-Au-Hemin-MIL-DNAzyme probe (curve f), the current signal rises instead, because the AuNPs and the MOF material in the probe have good conductivity, and the electrode interface electron conduction has a reinforcing effect. After the final PSA incubation step (curve g), the current signal was attenuated due to the binding between the PSA and its aptamer such that the probe was detached from the electrode interface. The above changes of peak current signals and the redox potential differences confirm the successful construction of the ECL sensor.

Furthermore, the Nyquist plots of EIS spectra can be used to display the changes during sensor construction. As shown in Fig. 3B, R_{et} represents the electron transfer resistance, which is expressed in the graph as the semicircle diameter of each curve. It can be seen that the impedance curve of the bare electrode (curve a) is almost a straight line, the R_{et} is very small, indicating that the bare electrode has a good electron conductivity. After the quantum dot was modified, R_{et} increases (curve b) because of the semiconducting properties of the quantum dot. With the gradual modification of cDNAs, PSA aptamers, and blocking agents (curves c, d, e), R_{et} also gradually increases due to the blocking effect of the biological sample. When the electrode is modified with a pDNA-Au-Hemin-MIL-DNAzyme probe (curve f), R_{et} decreases sharply because the conductivity of the Au NPs and the MOF material enhances the electron transfer efficiency on the electrode interface. After the final modification of the PSA (curve g), the pairing of the probe with the aptamer was disrupted through the competitive process, resulting in the detachment of the good conductor from the surface of the electrode and thus the R_{et} increased again. The above results in keeping with the results of the CV test prove the successful assembly of the ECL sensor.

A cathodic ECL signal (~ −1.5 V) from QDs and a anodic ECL signal from luminol (~ +0.45 V) were observed simultaneously. The possible reaction mechanism of the dual-potential is shown in Fig. S8 and S9. It is worth emphasizing that the introduction of pDNA-Au-Hemin-MIL-DNAzyme composites can effectively promote the performance of RECL assay when compared with the use of single material. As displayed in Fig. 3C, the quenched ECL signal of QDs (~ −1.5 V) and the enhanced ECL signal of luminol (+0.45 V) showed an “off-on” state before the target PSA was added, and the value of ECL_{QDs}/ $ECL_{Luminol}$ was determined to be about 0.17, which attributed to multiple catalytic reactions and quenching effect from pDNA-Au-Hemin-MIL-DNAzyme; after the PSA was added, ascribing to the binding of PSA with aptamer which caused the disassembly of pDNA-Au-Hemin-MIL-DNAzyme bioconjugate from the electrode, cause their ECL signals to switch from the “off-on” state to the “on-off” state, and the value of ECL_{QDs}/ $ECL_{Luminol}$ was calculated to be 5, indicating successful preparation of the

ratiometric ECL aptasensor. In addition, Fig. 3D shows the signal stability of the ratiometric aptasensor during the 20 cycles of ECL test from + 0.5 to − 1.5 V. The ECL signals of QD and luminol fluctuate slightly within a narrow range, and the intensity ratio ($ECL_{QDs}/ECL_{Luminol}$) is relatively constant (RSD = 3.1%), indicating that the ratiometric aptasensor is relatively stable.

3.3. Optimization of the experimental conditions

The optimization of the incubation time and the scanning rate were investigated before. As shown in Fig. S10A, with the increase of the incubation time, the ECL ratio shows an upward trend. After incubation for 60 min, the ECL ratio value has tiny changes, indicating that the optimal incubation time for PSA is 60 min, and the process of aptamer binding to release the probe has reached a steady state. Therefore, set the PSA incubation time to 60 min during the subsequent testing. In testing process, we performed optimization of the scanning rate. The same group of electrodes were tested for ECL at window rates of 0.1, 0.2, 0.3, 0.4, and 0.5 V/s, respectively. The optimization results are shown in Fig. S10B. When the rate is 0.3 V/s, the ECL ratio is highest, indicating that 0.3 V/s is the optimal scanning rate within the operating range.

3.4. ECL detection of PSA

In order to further improve the sensitivity and accuracy of the sensor, the ECL scanning rate and the incubation time of the PSA were first optimized before the sample was tested. The analytical performance of the approach was characterized under optimal experimental conditions. To evaluate the effect of this sensor on the detection of PSA, a series of different concentrations of PSA samples were tested in this work. As shown in Fig. 4C, under the optimal detection conditions, with the increase of the PSA concentration, the ECL signal of the QDs increases and the ECL signal of the luminol decreases simultaneously. The value of $ECL_{QDs}/ECL_{Luminol}$ was linearly dependent on the logarithm of PSA concentration in the range between 0.5 ng mL^{-1} and 500 ng mL^{-1} (Fig. 4A). The linear regression equation is $R_{ECL}(au) = 1.2096 \log C_{PSA} + 1.00095$ with the correlation coefficient of 0.9977. The R_{ECL} represents the ratio of $ECL_{QDs}/ECL_{Luminol}$ and C_{PSA} represents the concentration of PSA. Fig. 4B shows the approximated linear relation results between the $ECL_{Luminol}/ECL_{QDs}$-$\log C_{PSA}$ and $ECL_{QDs}/ECL_{Luminol}$-$\log C_{PSA}$, indicating the ratiometric ECL aptasensor has good assay performance. To prove the superior precision of the dual-signal detection mode, Fig. 4D and Fig. 4E displays the ECL single-signal detection results and respective calibration curves of QDs and luminol. The correlation coefficient were respectively calculated to be 0.9716 and 0.9460. It is worth to note that the ratiometric assay promoted the detection performance of the ECL aptasensor.

3.5. Specificity, reproducibility, and stability of the aptasensor

To investigate the selectivity of the aptasensor, equal amounts of PSA and various interfering agents including bovine serum albumin (BSA), streptavidin (SA), human immunoglobulin (IgG), adenosine triphosphate (ATP), and mixed samples (PSA: BSA: SA: IgG: ATP = 20%: 20%: 20%: 20%: 20%) were used to construct a ratiometric ECL sensor. Each group of experiments was performed in parallel three times (Fig. 4F). Two larger values of $ECL_{QDs}/ECL_{Luminol}$ can be obtained after the addition of PSA or the mixture, while only very weak intensity ratios emerged after the addition of IgG, BSA, ATP and SA. Additionally, the two stronger ECL signals resulted from the addition of PSA and the mixture were fitted to the linear regression equation. The

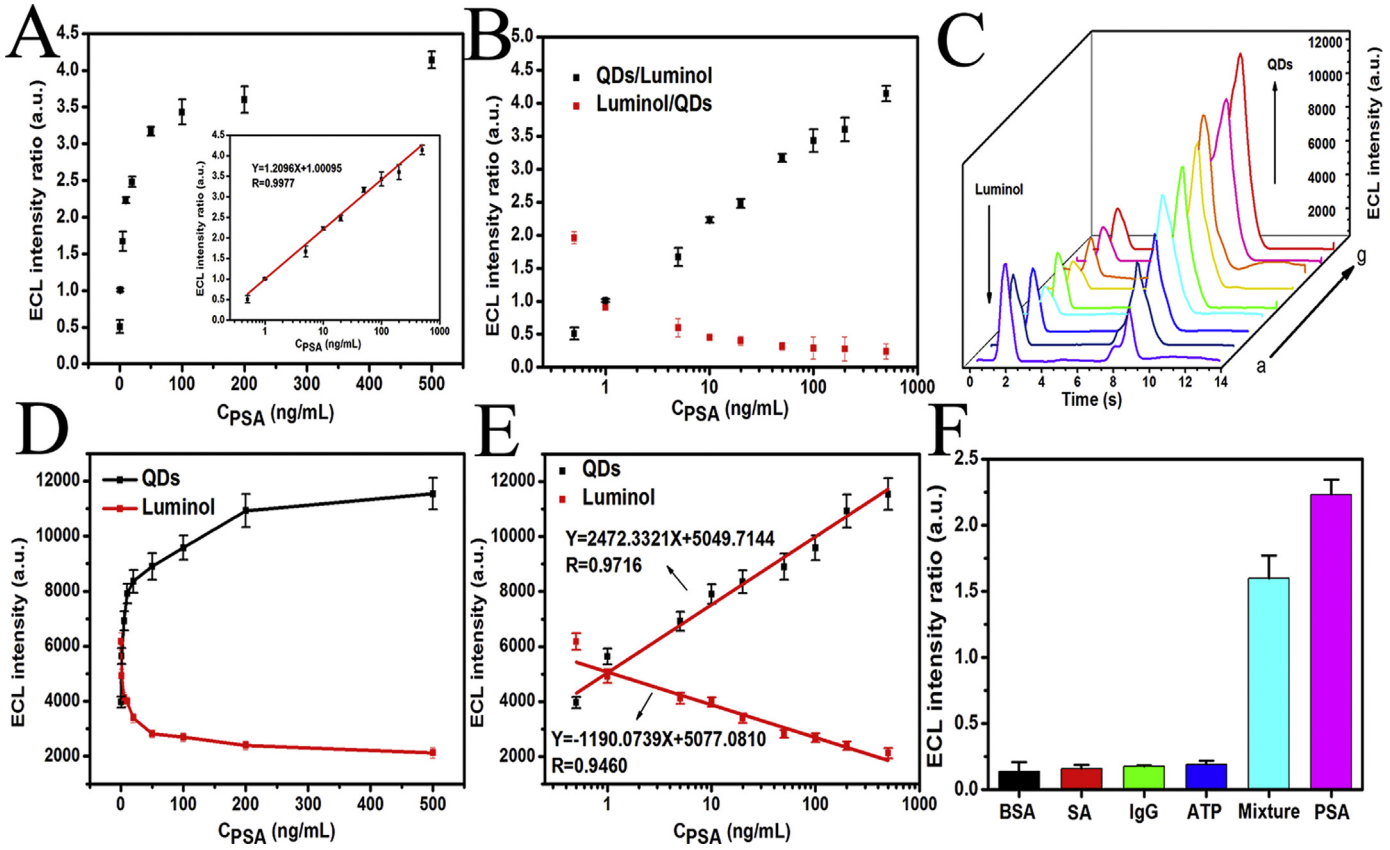

Fig. 4. (A) Calibration curve of $ECL_{QDs}/ECL_{Luminol}$. (B) Dual-signaling ECL intensity ratio of QDs and luminol, (C) ECL profiles, (D) Single-signaling ECL intensities of QDs and luminol and (E) Calibration curve of $ECL_{luminol}$ and ECL_{QDs} for determining different concentration of the PSA from 0.5 to 500 ng mL^{-1}. (F) Selectivity of the proposed electrochemiluminescence aptasensor. The concentrations of IgG, ATP, SA, BSA and PSA are 10 ng mL^{-1}.

Table 1
Determination of PSA in human blood serum (n = 3) with the proposed ECL aptasensor.

Serum sample	concentration of PSA added (ng mL^{-1})	Concentration obtained with immunosensor (ng mL^{-1})	Recovery(%)	RSD(%)
1	10	10.21	102.1	5.1
2	20	19.48	97.4	1.2
3	50	51.7	103.0	3.0

result shows that based on the specific recognition of PSA and its aptamers, the ratiometric sensor has the ability to specifically detect PSA.

The reproducibility experiment was tested by comparing within groups and between groups. It can be found that the sensor shows acceptable reproducibility by comparing the results of five groups of sensor tests (RSD = 4.2%). In addition, the ratiometric ECL sensors that stored in a 4 °C refrigerator for 5 days, 10 days, and 15 days were tested and can still retain more than 87.8% of the original ECL signals (RSDs varied from 6.4% to 10.1%), demonstrating the aptasensor with good stability (Fig. S11).

3.6. Analysis of clinical serum specimens

We evaluated the recovery in different concentrations of PSA solutions diluted in a healthy human serum sample. The experiment was done in parallel with at least three groups. The results are presented in Table 1. The recovery rates of the serum samples ranged from 97.4% to 103.0% and RSDs varied from 1.2% to 5.1%, thereby validating the reliability and practicality of this method. Table S1 shows the comparison between the proposed NECL aptasensor and some other ECL aptasensor in the visible range for detection of PSA. These results suggested that the biosensor has a promising potential application prospect for the detection of PSA in clinical diagnosis.

4. Conclusions

In this work, a signal-amplified NIR ratiometric ECL detection strategy was developed based on the MOF/Au/G-quadruplex with both quenching and enhancement effects. To maximize the signal-to-noise ratio, four conclusions could be drawn for the novel ratiometric ECL strategy: (i) NIR ECL emitter can minimize autofluorescence of serum; (ii) two separate ECL signals located in cathode and anode can avoid disadvantageous cross-reaction and signal overlap; (iii) most interferences can be eliminated by built-in self-calibration of two ECL signals; (iv) the synergetic effect of MOF/Au/G-quadruplex can greatly enhance the intensity ratio of the two ECL emitters. The proposed sensing mode has a certain guiding role in the construction of other amplified ratiometric ECL sensors. However, the ECL sensing strategy only tested PSA samples using standard recovery experiment, it is still necessary to further study its practical effects in clinical application.

Acknowledgments

We gratefully acknowledge the financial support from National Natural Science Foundation of China (21375043) and Sci-tech Innovation Foundation of Huazhong Agricultural University (2662017PY042).

Appendix A. Supporting information

Supplementary data associated with this article can be found in the online version at doi:10.1016/j.bios.2018.07.029.

References

Cao, Y., Yuan, R., Chai, Y., Mao, L., Niu, H., Liu, H., Zhuo, Y., 2012. Biosens. Bioelectron. 31 (1), 305–309.
Chen, H., Zhang, H., Yuan, R., Chen, S., 2017. Anal. Chem. 89 (5), 2823–2829.
Chen, Z., He, X., Wang, Y., Wang, K., Du, Y., Yan, G., 2013. Biosens. Bioelectron. 41, 519–525.
Cheng, Y., Huang, Y., Lei, J., Zhang, L., Ju, H., 2014. Anal. Chem. 86 (10), 5158–5163.
Dennany, L., Innis, P.C., Wallace, G.G., Forster, R.J., 2008. J. Phys. Chem. B 112 (41), 12907–12912.
Fang, J.M., Leng, F., Zhao, X.J., Hu, X.L., Li, Y.F., 2014. Analyst 139 (4), 801–806.
Feng, Q.-M., Shen, Y.-Z., Li, M.-X., Zhang, Z.-L., Zhao, W., Xu, J.-J., Chen, H.-Y., 2016a. Anal. Chem. 88 (1), 937–944.
Feng, S., Zheng, Z., Xu, Y., Lin, J., Chen, G., Weng, C., Lin, D., Qiu, S., Cheng, M., Huang, Z., Wang, L., Chen, R., Xie, S., Zeng, H., 2017. Biosens. Bioelectron. 91, 616–622.
Feng, X., Gan, N., Zhang, H., Li, T., Cao, Y., Hu, F., Jiang, Q., 2016b. Biosens. Bioelectron. 75, 308–314.
Fu, X., Tan, X., Yuan, R., Chen, S., 2017. Biosens. Bioelectron. 90, 61–68.
Gerhard, M., Juhl, H., Kalthoff, H., Schreiber, H.W., Wagener, C., Neumaier, M., 1994. J. Clin. Oncol. 12 (4), 725–729.
Hao, N., Li, X.-L., Zhang, H.-R., Xu, J.-J., Chen, H.-Y., 2014. Chem. Commun. 50 (94), 14828–14830.
Jayanthi, V.S.P.K.S.A., Das, A.B., Saxena, U., 2017. Biosens. Bioelectron. 91, 15–23.
Jiang, X., Chai, Y., Wang, H., Yuan, R., 2014. Biosens. Bioelectron. 54, 20–26.
Lang, Q., Wang, F., Yin, L., Liu, M., Petrenko, V.A., Liu, A., 2014. Anal. Chem. 86 (5), 2767–2774.
Lei, J., Ju, H., 2012. Chem. Soc. Rev. 41 (6), 2122–2134.
Li, F., Cui, H., 2013. Biosens. Bioelectron. 39 (1), 261–267.
Li, Y.-J., Ma, M.-J., Zhu, J.-J., 2012. Anal. Chem. 84 (23), 10492–10499.
Liu, K., Zhang, J.-J., Wang, C., Zhu, J.-J., 2011. Biosens. Bioelectron. 26 (8), 3627–3632.
Miao, H., Wang, L., Zhuo, Y., Zhou, Z., Yang, X., 2016. Biosens. Bioelectron. 86, 83–89.
Perfezou, M., Turner, A., Merkoci, A., 2012. Chem. Soc. Rev. 41 (7), 2606–2622.
Qi, W., Wu, D., Zhao, J., Liu, Z., Zhang, W., Zhang, L., Xu, G., 2013. Anal. Chem. 85 (6), 3207–3212.
Roggan, A., Friebel, M., Dorschel, K., Hahn, A., Muller, G., 1999. J. Biomed. Opt. 4 (1), 36–46.
Rong, Q., Feng, F., Ma, Z., 2016. Biosens. Bioelectron. 75, 148–154.
Shao, K., Wang, B., Ye, S., Zuo, Y., Wu, L., Li, Q., Lu, Z., Tan, X., Han, H., 2016. Anal. Chem. 88 (16), 8179–8187.
Shao, K., Wang, J., Jiang, X., Shao, F., Li, T., Ye, S., Chen, L., Han, H., 2014. Anal. Chem. 86 (12), 5749–5757.
Shao, K., Zhang, C., Ye, S., Cai, K., Wu, L., Wang, B., Zou, C., Lu, Z., Han, H., 2017. Sens. Actuators B-Chem. 240, 586–594.
Sun, S., Sun, W., Mu, D., Jiang, N., Peng, X., 2015. Chem. Commun. 51 (13), 2529–2531.
Tian, D., Duan, C., Wang, W., Cui, H., 2010. Biosens. Bioelectron. 25 (10), 2290–2295.
Wang, H.-S., Liu, H.-L., Wang, K., Ding, Y., Xu, J.-J., Xia, X.-H., Chen, H.-Y., 2017a. Anal. Chem. 89 (21), 11366–11371.
Wang, Y.-Z., Hao, N., Feng, Q.-M., Shi, H.-W., Xu, J.-J., Chen, H.-Y., 2016. Biosens. Bioelectron. 77, 76–82.
Wang, Y.-Z., Xu, C.-H., Zhao, W., Guan, Q.-Y., Chen, H.-Y., Xu, J.-J., 2017b. Anal. Chem. 89 (15), 8050–8056.
Wang, Y.L., Liu, F.R., Cao, J.T., Ren, S.W., Liu, Y.M., 2017c. Biosens. Bioelectron. 102, 525–530.
Wu, J., Fu, Z., Yan, F., Ju, H., 2007. Trend Anal. Chem. 26 (7), 679–688.
Wu, P., Hou, X., Xu, J.-J., Chen, H.-Y., 2016. Nanoscale 8 (16), 8427–8442.
Xie, S., Ye, J., Yuan, Y., Chai, Y., Yuan, R., 2015. Nanoscale 7 (43), 18232–18238.
Xu, S., Liu, Y., Wang, T., Li, J., 2011. Anal. Chem. 83 (10), 3817–3823.
Zhang, H.-R., Wang, Y.-Z., Zhao, W., Xu, J.-J., Chen, H.-Y., 2016. Anal. Chem. 88 (5), 2884–2890.
Zhang, H.-R., Xu, J.-J., Chen, H.-Y., 2013. Anal. Chem. 85 (11), 5321–5325.
Zhao, H.-F., Liang, R.-P., Wang, J.-W., Qiu, J.-D., 2015. Chem. Commun. 51 (63), 12669–12672.